Zhu, F. & Zhao, J. (2019). *Géotechnique* **69**, No. 6, 526–540 [https://doi.org/10.1680/jgeot.17.P.274]

A peridynamic investigation on crushing of sand particles

F. ZHU* and J. ZHAO†

Particle crushing underpins important macroscopic behaviour of granular materials such as yielding, deformation, dilatancy, failure, mobility and packing features. The crushing condition and crushing pattern have commonly been examined for particles subjected to uniaxial loadings. In the real engineering context, a sand grain is typically in contact with several surrounding particles and is hence subjected to multi-directional loadings, a critical condition that has not been well accounted for in most crushing criteria and studies of crushing patterns relevant to discrete-based sand modelling. In this study, the crushing of single sand particles under different loading conditions is examined based on peridynamic simulations. The peridynamic method is found capable of realistically capturing the crushing of a sand particle under uniaxial loadings in terms of crushing load and the crushing pattern observed in experiments, and is able to simulate multi-contact particle crushing where experimental data are relatively scarce. By examining existing crushing criteria, it is found that the numerical results on the crushing load under multiple contacts compare favourably with the maximum contact force criterion, which states that particle crushing occurs when the maximum contact force reaches a threshold. It is observed that the number of child particles after the crushing of a sand particle bears no apparent correlation with the coordination number. The volumes of child particles can be statistically described by a normal or gamma distribution. The findings from the study offer insights into the behaviour of sand particle crushing, which can be useful for future discrete modelling of granular sand where crushing is important.

KEYWORDS: failure; numerical modelling; particle crushing/crushability; particle-scale behaviour; sands

INTRODUCTION

The discrete-element method (DEM) (Cundall & Strack, 1979) prevails in discrete modelling of granular materials. While unbreakable particles are commonly considered in DEM simulations, the capacity of modelling particle crushing in DEM is desirable in many practical applications, particularly when particle crushing is an important factor altering the macroscopic behaviour of a granular material. In the past, crushing of particles has typically been handled using two major approaches in DEM modelling. One introduces clusters of smaller particles (Cheng *et al*., 2003; Wang & Yan, 2011; Cil & Alshibli, 2012; Li *et al*., 2013), whereas the other replaces an individual particle by several child particles with fixed topological characteristics a priori when a pre-set crushing criterion is met (Lobo-Guerrero & Vallejo, 2005; Brosh *et al*., 2011). The particle replacement approach has been frequently adopted owing to its relatively high computational efficiency as compared to the cluster method. However, immediate questions arising from the particle replacement approach include the selection of the crushing criterion and the number and size of child particles, which appear to be rather arbitrary in many studies. There have been a variety of crushing criteria adopted or discussed in past studies, such as the octahedral shear stress (OSS) criterion (McDowell & de Bono, 2013), maximum contact force (MCF) criterion (Couroyer *et al*., 2000; Hanley *et al*., 2015), mean and major principal stress criteria (de Bono & McDowell, 2016) and maximum tensile stress (MTS) criterion (Lobo-Guerrero & Vallejo, 2005). Moreover, the crushing threshold of a single particle may also be expressed in terms of energy (Yashima *et al*., 1987; Tavares & King, 1998). The use of different criteria may lead to a significant difference in the predicted crushing load, creating confusion for both researchers and engineers. Moreover, the number and size of child particles after crushing, in other words the crushing pattern, have often been chosen in a rather arbitrary manner. Two to four equal-sized child particles were used by McDowell & de Bono (2013) to model particle breakage, whereas Lobo-Guerrero & Vallejo (2005) assumed that one particle could break into eight child particles with different sizes. There have been attempts using ten or more child particles (Tsoungui *et al*., 1999; Zhou *et al*., 2014; Cil & Buscarnera, 2016). The various simplifications may lend great convenience in modelling the crushing process, but lack adequate scientific justifications and verifications.

Experimental tests on the crushing behaviour of sand particles have been predominantly based on single sand particles (Nakata *et al*., 1999, 2001; McDowell, 2002; Cil & Alshibli, 2012; Wang & Coop, 2016). Frequently, these experiments were performed by compressing a particle under uniaxial loadings between two parallel platens. The strength of a single particle was typically measured by the MCF recorded on the platens, or according to a nominal strength defined by dividing the MCF with the particle diameter squared (Jaeger, 1967). Under uniaxial loading conditions, it is widely agreed that a particle crushes as a result of tension failure. Zhao *et al*. (2015) studied the crushing pattern of single sand particles using X-ray micro-tomography techniques. The crushing pattern can be exceedingly complex, depending on the morphology and microstructure of the tested particle. A sphere-like particle with relatively good material uniformity typically breaks into several ‘orange slice’ child particles

Manuscript received 31 October 2017; revised manuscript accepted 4 May 2018. Published online ahead of print 13 August 2018.
Discussion on this paper closes on 1 November 2019, for further details see p. ii.
* Department of Civil and Environmental Engineering, The Hong Kong University of Science and Technology, Hong Kong SAR, P. R. China.
† Department of Civil and Environmental Engineering, The Hong Kong University of Science and Technology, Hong Kong SAR, P. R. China (Orcid:0000-0002-6344-638X).

under uniaxial loadings (Zhao *et al.*, 2015). However, a mismatch is apparent between the experimental uniaxial loading condition and general engineering conditions where a particle is subjected to multi-directional loadings. Evidently, multiple contacts and multi-directional loading conditions may lead to a greatly complicated internal stress field where both tension and shear effects can present, and it is often difficult to judge which factor governs the occurrence of crushing. It is questionable whether the crushing force obtained from uniaxial crushing tests on a particle can be directly used to estimate its strength under multi-directional loading conditions. Moreover, a particle is unlikely to break into a few 'orange slices' under multi-directional loadings. Experimental studies exploring the crushing of a sand grain under multi-directional loading conditions are scarce, probably owing to the considerable difficulties in setting up such tests and taking adequate measurements. Notably, Todisco *et al.* (2017) extended crushing tests to four-point and six-point loading conditions by compressing a particle placed between fixed steel balls or other particles. They found that more contacts generally resulted in a higher failure stress level inside a particle. The test results, however, still appear to be insufficient if one wants to establish a quantitative crushing criterion for single particles under multi-directional loadings, as the forces are measured at the steel mounts but not at individual contact points.

The lack of experimental data prevents direct verifications of the assumed particle crushing criteria and crushing patterns under multi-directional loading conditions. Indirect ways have therefore been proposed to examine those assumptions based on macroscopic experimental results. McDowell & de Bono (2013) found that using the OSS crushing criterion and assuming one particle breaks into two to four equal-sized child particles, one could obtain the correct macroscopic behaviour of sand under one-dimensional compression. By further examining several other crushing criteria using DEM, de Bono & McDowell (2016) suggested that both the OSS criterion and MCF criterion might offer reasonable predictions on the macroscopic crushing behaviour of sand. These studies provide useful guidance on selecting the proper crushing criterion and crushing patterns, but do not offer compelling evidence as to why a certain crushing criterion and crushing pattern may apply.

The lag in experimental progress does not stop attempts at numerical simulations of particle crushing. Using the traditional DEM, it is possible to model a particle as an agglomerate of bonded elementary spheres, and compress it until crushing (Cheng *et al.*, 2003; Li *et al.*, 2013; Cil & Alshibli, 2014). Such an approach is successful in modelling particle crushing under uniaxial compression, but possesses some drawbacks. One apparent drawback is that it requires careful calibration on parameters of the bonds between the elementary spheres. Those bonds do not exist in reality and are merely a numerical approach to model intact material. Consequently the parameters of the bonds, including the stiffness and strength, are numerical quantities but not material properties in their nature, and should be calibrated by faithful data, ideally experimental records. The parameters calibrated from experimental data under one loading condition are not guaranteed to be applicable under other conditions. It should be realised that the DEM is essentially a discrete tool for modelling granular materials, and may not be suitable to model a single and intact particle before and during breakage. From this point of view, it is desirable to employ a continuum-based tool that is capable of handling the fracturing process during crushing.

In this paper, a relatively new method is employed, namely peridynamics (Silling, 2000; Silling *et al.*, 2007), to model the crushing process of single sand particles. The method is distinguished by its capability in handling discontinuities such as fractures and cracks. It has recently been extended to modelling a variety of materials with brittle fracture behaviours, including concrete (Huang *et al.*, 2015), rock (Rabczuk & Ren, 2017; Zhou & Shou, 2017), ceramic (Lai *et al.*, 2018), glass (Kilic & Madenci, 2009) and ice (Liu *et al.*, 2017). A comprehensive review of the peridynamic method with benchmark models can be found in Madenci & Oterkus (2014). The method is advantageous over other traditional methods in many aspects of solving fracture-related problems. For instance, the extended finite-element method (XFEM), a continuum-based method commonly adopted for simulating fractures, is known to have not been well developed to handle cracks in a three-dimensional (3D) domain with complex loading conditions, and requires external interference to guide the growth of cracks (Bouchard *et al.*, 2003; Baydoun & Fries, 2012). Handling multiple crack growth and crack branching in XFEM requires extra effort, such as introducing additional enrichment functions (Daux *et al.*, 2000; Xu *et al.*, 2014) and such techniques have not been well established for 3D domains. In contrast, the peridynamic method inherently adapts to complex geometries and loading conditions and employs a single criterion to capture the initiation and propagation of cracks. In this paper it is demonstrated that the peridynamic method is capable of simulating a single sand particle crushing phenomenon. The simulations offer insights into the crushing behaviour of single sand particles, provide a scientific basis for the study of crushing criteria and crushing patterns, and facilitate modelling of particle crushing with the framework of traditional discrete methods.

THE PERIDYNAMIC METHOD

Basic theory

Peridynamics is a non-local, continuum-based, mesh-free method first introduced by Silling (2000). In this method, a continuous material body (such as grain) is discretised into elements and each element is represented by a material point with assigned volume and mass. A material point interacts with others within its family through peridynamic bonds. The extent of the family is defined by a parameter 'horizon' which is typically a radius as illustrated in Fig. 1(a). All material points within the family of $\boldsymbol{x}$ are called the 'neighbourhood' of $\boldsymbol{x}$. For intact material without defect, peridynamic bonds are established between a material point and each of its neighbourhood points.

Peridynamics is different from classical continuum methods such as the finite-element method (FEM) in the sense that its basic equation is in integration form rather than partial differential form. The method is therefore inherently capable of handling discontinuities such as cracks inside a continuum material. In this study, the authors adopted the 'ordinary state-based peridynamics' (Silling *et al.*, 2007) for which the basic equation can be expressed by

$$\rho(\boldsymbol{x})\ddot{\boldsymbol{u}}(\boldsymbol{x},\,t) = \int_{\mathcal{H}_x} [\boldsymbol{T}(\boldsymbol{x},\,t) < \boldsymbol{x}' - \boldsymbol{x} > - \boldsymbol{T}(x',t) < \boldsymbol{x} - \boldsymbol{x}' >]\mathrm{d}V_{x'} + \boldsymbol{b}(\boldsymbol{x},\,t) \tag{1}$$

where $\rho(\boldsymbol{x})$ represents the density at material point $\boldsymbol{x}$; $\boldsymbol{u}(\boldsymbol{x},\ t)$ is the displacement of material point $\boldsymbol{x}$ at time t; $\boldsymbol{b}$ represents a body force density; and $\mathcal{H}_x$ represents the family of a material point $\boldsymbol{x}$ defined by a horizon δ. In principle, the horizon δ should be chosen sufficiently large so that crack branching can be correctly captured (Silling & Askari, 2005; Ha & Bobaru, 2010), since a large horizon would include a sufficient number of directions where the crack can develop. Increasing the horizon size does not alter the results in general but requires

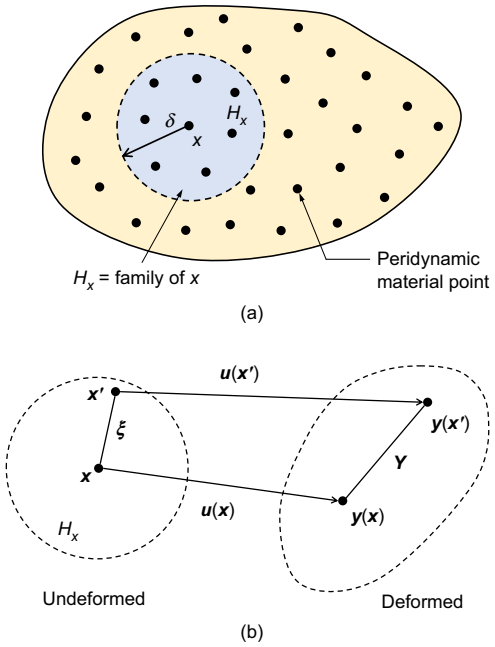

Fig. 1. Schematic illustration: (a) a peridynamic domain and the family of a material point x; (b) bond vector ξ, displacement vector u and deformation state Y

higher computational cost (Ha & Bobaru, 2010). However, an exceedingly large horizon may induce excessive wave dispersion (Silling & Askari, 2005) and should also be avoided. In this study, δ for the particle has been specified to be twice the size of the discretised tetrahedron elements, corresponding to a number of neighbourhoods of approximately 300 to 400. The selected δ is slightly larger than commonly adopted values (c.f. Ha & Bobaru, 2010; Liu *et al.*, 2017; Rabczuk & Ren, 2017; Lai *et al.*, 2018), while far from being exceedingly large (Madenci & Oterkus, 2014). A peridynamic force state $\boldsymbol{T}$ is defined to compute the force density (per unit volume squared) at each bond. A variety of material constitutive models can be implemented with properly adopted functions for the force state $\boldsymbol{T}$. For the sand particles studied in this paper, a linear peridynamic solid (LPS) material model (Silling *et al.*, 2007) was adopted. The model is a non-local analogue to the classical linear elastic material model. In the LPS model, the force state $\boldsymbol{T}$ is computed by

$$\boldsymbol{T} = \underline{t}\frac{\boldsymbol{Y}}{\|\boldsymbol{Y}\|} \tag{2}$$

$$\underline{t} = \frac{3K\theta}{m\langle \boldsymbol{x}\rangle}\omega\underline{x} + \frac{15\mu}{m\langle \boldsymbol{x}\rangle}\omega e^{d} \tag{3}$$

where $\boldsymbol{Y} = \boldsymbol{\xi} + \boldsymbol{u}(\boldsymbol{x}', t) - \boldsymbol{u}(\boldsymbol{x}, t)$ represents the deformation state as illustrated in Fig. 1(b) and the undeformed bond vector $\boldsymbol{\xi}$ is defined by $\boldsymbol{\xi} = \boldsymbol{x}' - \boldsymbol{x}$. Bond forces are computed in a scalar force state $\underline{t}$, in which μ and K represent shear and bulk modulus, respectively, $\underline{x}$ is a position scalar state whose value at bond $\boldsymbol{\xi}$ equals $\|\boldsymbol{\xi}\|$, and $m\langle \boldsymbol{x}\rangle$ defines a weighted volume at material point $\boldsymbol{x}$ and can be calculated by

$$m\langle \boldsymbol{x}\rangle = \int_{\mathcal{H}_x} \omega\|\boldsymbol{\xi}\|^2 \,\mathrm{d}V_{x'} \tag{4}$$

where ω is an influence function taken as one in this study as it gives reasonable results. Selection of the influence function remains an active research field, although a unity influence function has often been used (Warren *et al.*, 2009; Liu *et al*, 2017). Nonetheless, a recent study has indicated that a unity influence function in the LPS model may result in inaccuracy near the material boundary (Mitchell *et al.*, 2015) and a fine mesh is necessary to minimise such effect. A dilation θ is defined as

$$\theta\langle \boldsymbol{x}\rangle = \frac{3}{m\langle \boldsymbol{x}\rangle}\int_{\mathcal{H}_x} \omega\|\boldsymbol{\xi}\|\underline{e}\,\mathrm{d}V_{x'} \tag{5}$$

where $\underline{e} = \|\boldsymbol{Y}\| - \|\boldsymbol{\xi}\|$ is an extension scalar state representing the extension of a bond and can be divided into an isotropic part $\underline{e}^{\mathrm{i}} = \theta\langle \boldsymbol{x}\rangle\underline{x}/3$ and a deviatoric part $\underline{e}^{\mathrm{d}} = \underline{e} - \underline{e}^{\mathrm{i}}$. As shown in equation (3), the LPS model is structurally analogous to the classical linear elastic material model. The LPS model, together with the critical stretch damage model introduced below, has been employed in this study to simulate silica sand with an elastic brittle fracture behaviour.

Damage model

In peridynamics the damage of material is modelled by the failure of bonds. A damage model should be selected based on the nature of material to be modelled. Here the authors employed a critical stretch damage model (Parks *et al.*, 2012) to simulate the brittle breakage of sand particles. When a bond between two material points is stretched to a critical strain of s_{c}, the bond is considered broken and no longer carries any force. The load originally carried by the bond will be redistributed to its neighbouring bonds. This process may result in successive breakage of other bonds and eventually form progressive damage. The breakage of bonds is irreversible, so a broken bond cannot be re-established between two material points. The critical stretch value of the bond is derived based on the energy required to create new material surfaces (Madenci & Oterkus, 2014) and can be written in the following form

$$s_{\mathrm{c}} = \sqrt{\frac{G_{\mathrm{c}}}{\left\{3\mu + (3/4)^4[K - (5\mu/3)]\right\}\delta}} \tag{6}$$

where δ represents the horizon as illustrated in Fig. 1(a); G_{c} represents the critical energy release rate, which can be obtained from experimental tests for a specific material. For silica, the critical energy release rate is found to be typically between 0·5 and 23 J/m^2 (Brace & Walsh, 1962; Zeleny & Piret, 1962; Parks, 1984). A mid-range value of 10 J/m^2 is adopted for the analyses presented hereafter. The critical energy release rate, which represents a material property in its nature, is the only parameter needed in addition to the material constitutive parameters to simulate damage to the material. Hence the peridynamic method requires no external interference to guide the initiation of damage and propagation of cracks.

For each bond, a variable g is defined according to the status of the bond (Silling & Askari, 2005). An intact bond has a g value of one, whereas a broken bond has g equal to zero. At every material point, the damage ϕ is defined by

$$\phi(\boldsymbol{x}, t) = 1 - \frac{\int_{\mathcal{H}_x} g\langle \boldsymbol{\xi}\rangle \mathrm{d}V_{x'}}{\int_{\mathcal{H}_x} \mathrm{d}V_{x'}} \tag{7}$$

It is apparent that $\phi = 0$ indicates the intact condition of all bonds connecting to the material point, whereas $\phi = 1$ reflects that all connecting bonds are broken. The damage of material points provides a straightforward way to track the initiation and propagation of cracks.

Contact model

During compression, the load is applied through the loading platens. A contact model is required to simulate the

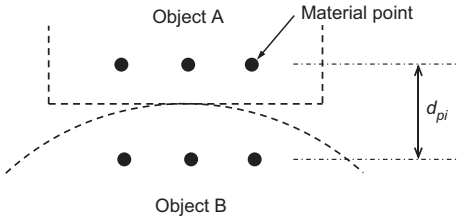

Fig. 2. Schematic illustration of the critical distance d_{pi} in contact model

interactions between the particle and loading platens. It is also needed to model the interactions (if any) between the broken pieces of a particle. The contact model introduced by Parks *et al.* (2012) is adopted in this paper. The model solves for contact force density $\boldsymbol{f}_s$ between two material points based on their relative positions, as presented by

$$\boldsymbol{f}_s = \min\left\{0,\ \frac{c_s}{\delta}(\|\boldsymbol{y}_p - \boldsymbol{y}_i\| - d_{pi})\right\}\frac{\boldsymbol{y}_p - \boldsymbol{y}_i}{\|\boldsymbol{y}_p - \boldsymbol{y}_i\|} \quad (8)$$

where $\boldsymbol{y}_p$ and $\boldsymbol{y}_i$ are positions of two material points p and i, respectively; d_{pi} represents the contact distance at which two points will be considered in touch, as illustrated in Fig. 2; and $c_s = 18k/\pi\delta^4$ where k represents the stiffness of contact. The above equation calculates a normal repulsive force density which tends to push two material points apart. If the relative movement of the contacting material points has a non-zero component perpendicular to the normal direction, a frictional force is applied along that tangential direction and it is defined by Coulomb's law $F_T = f F_N$, where F_N is the normal contact force and f is the coefficient of friction, which is specified to be 0·5 in this study.

NUMERICAL SIMULATIONS

Benchmark model

Crushing of a single sand particle under uniaxial loadings was first simulated to test the performance of the peridynamics method. The modelled particle was assumed to be typical silica sand and is isotropic, homogeneous and spherical with a diameter of 1·5 mm. Shear and bulk moduli of 43·5 GPa and 47·6 GPa (equivalent to a Young's modulus of 100 GPa and a Poisson ratio of 0·15) have been assumed for the particle, which are within the typical range for silica sand (Domenico, 1977; Spencer *et al.*, 1994; Holtzman *et al.*, 2009; Erdoğan *et al.*, 2017). Two stiff loading platens, as those used in particle crushing experiments (Zhao *et al.*, 2015), were modelled. The parameters used in the modelling are summarised in Table 1. The spherical domain of the particle was first discretised into

Table 1. Summary of adopted parameters in the peridynamic model

Parameter	Value
Density of sand: kg/m^3	2650
Shear modulus of sand: GPa	43·5
Bulk modulus of sand: GPa	47·6
Critical energy release rate of sand particle, G_c: J/m^2	10
Density of platen: kg/m^3	3850
Shear modulus of platen: GPa	155·7
Bulk modulus of platen: GPa	226·2
Particle–platen friction coefficient	0·5
Contact distance, d_{pi}: mm	0·05
Contact stiffness, k: GPa	500
Horizon (particle/platen): mm	0·2/0·1

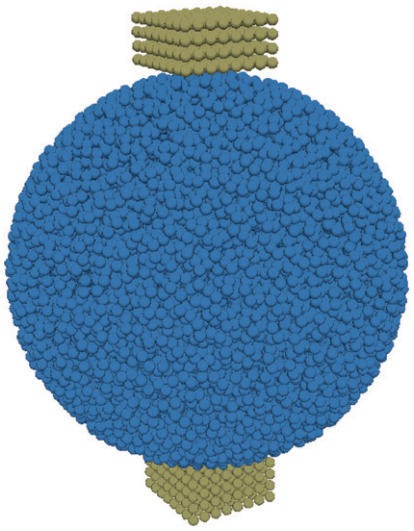

Fig. 3. Material points for peridynamic modelling of the particle and loading platens

tetrahedrons and the centroid of each tetrahedron was selected as a peridynamic material point. Each material point possesses the volume and mass of its corresponding tetrahedron. In this study, the discretisation was performed in a fine manner into nearly 20 000 material points with an average element size of approximately 0·09 mm (i.e. the average length of discretised tetrahedrons), although a parametric study for the modelled particle under uniaxial load has indicated that with discretised material points of 5000 to 20 000 the calculated crushing load is not apparently altered. The loading platens were discretised with a cubic pattern and an element size of 0·05 mm. The discretised particle and loading platens are shown in Fig. 3. Horizon values of 0·2 mm and 0·1 mm were specified for the particle and loading platens, respectively, corresponding to approximately twice the discretised element size. To simulate a brittle failure of a sand particle, a large contact stiffness of $k = 500$ GPa was selected. Such contact stiffness, as will be shown later, gives a reasonable stress–strain relation during the compression process. Owing to the limited scope of the current study, the effect of contact stiffness on crushing behaviour is not investigated herein and the contact stiffness was kept constant in all simulations.

To simulate the compression process, the two platens were set to move at a constant rate v of 0·1 m/s towards the centre of the particle. The adopted loading rate is higher than that in experiments in order to enhance computational efficiency. A parametric study has been performed to examine the effect of loading rate on the crushing load and crushing pattern. Different loading rates ranging from 0·01 m/s to 12 m/s were tested. Similar crushing patterns were found (e.g. three or four 'orange slices' pattern) for loading rates up to 5·0 m/s, whereas the crushing load was not apparently affected when $v \leq 2{\cdot}0$ m/s, as presented in Fig. 4. However, the force–displacement curve shows considerable oscillations when $v \geq 1{\cdot}0$ m/s, indicating strong dynamic effects in the loading process. A similar finding was reported by Cheng *et al.* (2003) in their DEM study that the crushing load is insensitive to the loading rate when it is lower than 1·0 m/s. The adopted loading rate of 0·1 m/s therefore helps to minimise dynamic effects in the loading process, while reducing the computational cost to an affordable level.

The recorded load–displacement curve for the top platen is shown in Fig. 5. The applied force increases non-linearly with the displacement of the platen. Small local spikes in the curve

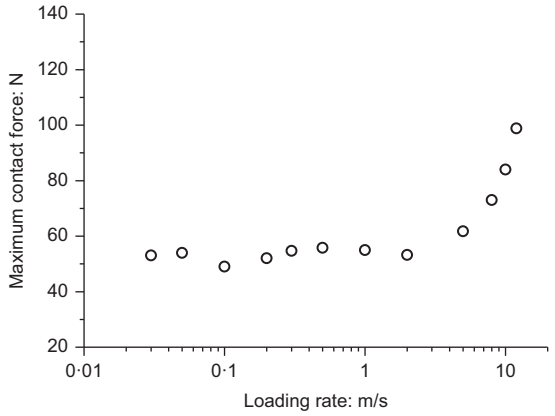

Fig. 4. Effects of loading rate on the crushing load

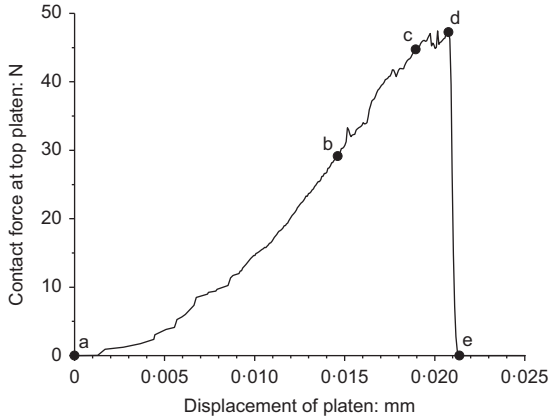

Fig. 5. Load–displacement curve of single sand crushing under uniaxial loading by peridynamic modelling (conditions of the particle at points a to e are shown in Fig. 7)

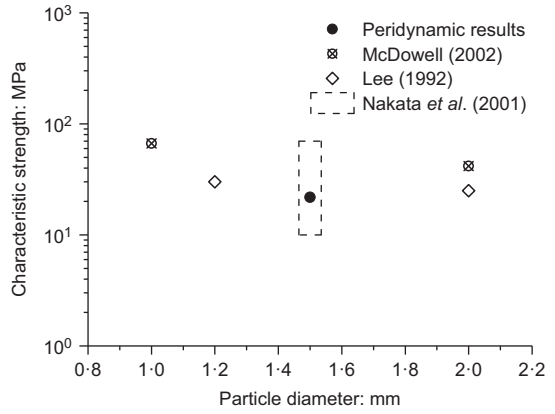

Fig. 6. Crushing strength of particle in comparison with experimental results

represent local damage and/or rotations of the particle. The MCF before crushing was found to be approximately 49 N. The characteristic strength, calculated by dividing the MCF by the square of particle diameter, was found to be approximately 22 MPa, falling well within the typical range obtained from experiments (Lee, 1992; Nakata *et al.*, 2001; McDowell, 2002) as shown in Fig. 6. It should be noted that the selection of critical energy release rate G_c does affect the crushing load of the particle. The adopted value of 10 J/m^2 herein is a mid-range value based on past experimental data.

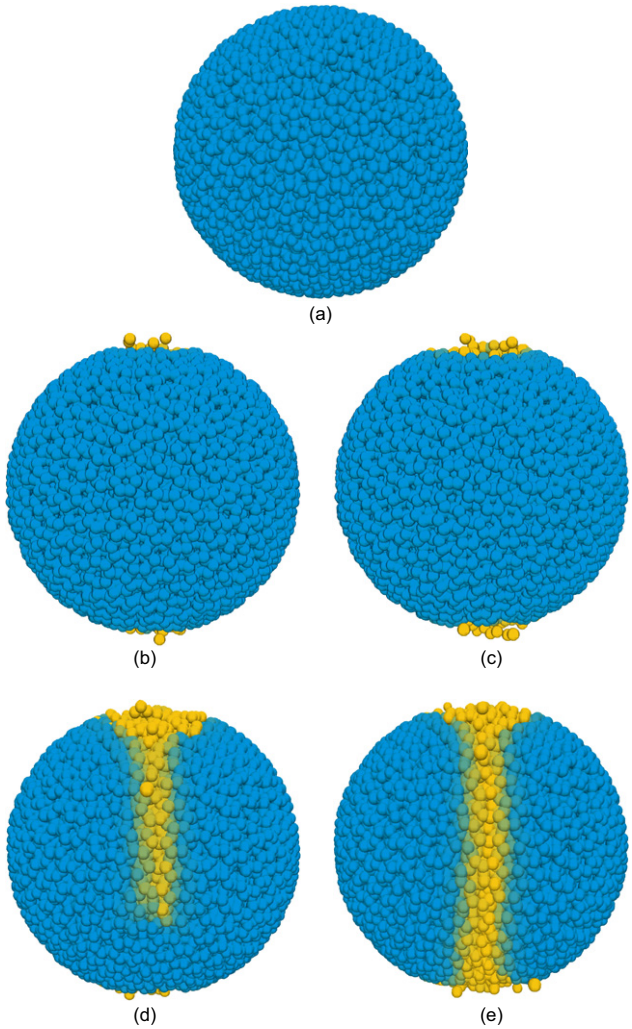

Fig. 7. Initiation of damage and formation of crack (side view): (a) initial condition; (b) local damage on top and bottom; (c) development of local damage; (d) formation of bulk crack; (e) split particle. Loading levels at conditions (a) to (e) are marked in Fig. 5. Some fully damaged material points are not shown for clarity

A higher or lower G_c may be adopted for a stronger or weaker particle, which will result in higher or lower crushing forces, to fit the upper and lower strength levels observed in experiments.

Figure 7 shows the initiation of damage and propagation of cracks in the particle. Damage of material points is shown in a different (lighter) shade to that of the main body of the particle. The damage initiates from the vicinity of the top and bottom contacts, which conforms to some analytical studies (Russell & Wood, 2009) and experimental observations (Gundepudi *et al.*, 1997; Salami *et al.*, 2015; Wang & Coop, 2016) on spheres/discs. Cracks were found incepted and propagated across the particle within a short duration. Two almost perpendicular crack planes were formed and split the particle into four similar 'orange slices', as shown by the top view in Fig. 8(a). Such a crushing pattern has been observed in many experimental studies for spheres crushed under uniaxial compression (Salman *et al.*, 1995; Antonyuk *et al.*, 2005). For natural sand particles, the morphology and micro-structures are often complex, leading to complex failure modes such as explosion and chipping (Wang & Coop, 2016). An experimental study comparable to the present numerical model was performed by Zhao *et al.* (2015) on Leighton Buzzard sand (LBS) particles, which mainly consist of quartz and possess good roundness without apparent micro-defects. A typical

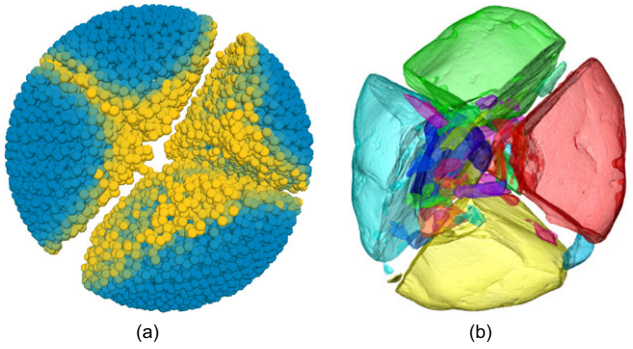

Fig. 8. Comparison of crushing patterns (a) from peridynamic modelling and (b) experimental record by Zhao *et al.* (2015) for a crushed LBS particle (top view)

splitting failure mode was observed in experiments with conchoidal fractures formed between the top and bottom contacts, as shown in Fig. 8(b). It can be seen that the peridynamic model captured the initiation of damage and the propagation of cracks in the particle, and reflected realistically the crushing pattern under uniaxial loadings. Therefore, the method was further extended to model the particle crushing phenomenon under complex loading conditions, for which experimental study is rare.

Crushing of single particle under multi-directional loadings

In engineering conditions, a particle is often subjected to multi-directional loadings, such as those shown in Fig. 9. Such a loading condition may induce complex stress fields inside the particle and create difficulties in determining the onset of crushing accurately. Various factors may affect the crushing load and the crushing pattern of a particle, the well-known ones include coordination number, locations of contacts and magnitude of contact forces. Beyond those, it was found that mineral hardness as well as particle shape at the contact locations also affect the crushing of a particle (Todisco *et al.*, 2017). To combine all factors in one study is practically challenging. In this paper the focus is placed on investigating particle crushing under varying coordination numbers, contact patterns and contact forces. The particle shape and stiffness at contacts are kept constant in all cases, with an acknowledgement that they may impose a certain impact on particle crushing behaviour, and such an effect may be investigated in future studies. The goal of the following work is to study the crushing load as well as the crushing pattern of particles under varied loading conditions using the peridynamic method, with a purpose to establish simplified rules that can facilitate traditional discrete modelling when consideration of particle crushing is demanded.

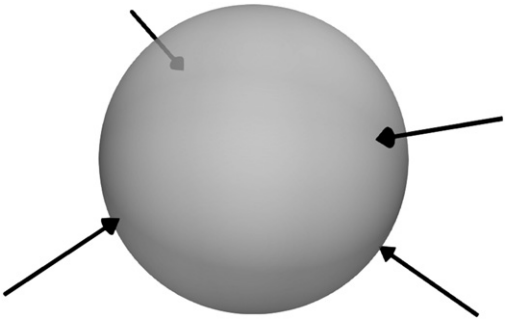

Fig. 9. A typical multiple-point loading configuration of a particle in an assembly

To cover a wide range of loading conditions, peridynamic models were created for particles with coordination numbers ranging from four to eight. Particles with fewer contacts are less likely to undergo crushing for reasons of stability. Higher coordination numbers may be possible, particularly for large particles, but the strong contacts (i.e. those that bear large forces and effectively contribute to the crushing of the particle) are always limited, as will be shown later. Observations from DEM simulations on sand assemblies following a similar grain size distribution to Toyoura sand (Guo & Zhao, 2013) rarely showed particles with more than eight major contact branches. Hence, consideration of a coordination number up to eight is expected to be adequate. For each coordination number case, different contact patterns were considered. To obtain random contact patterns, the authors simulated an assembly of uniformly sized spheres being poured into a container and settled under gravity, and extracted contact patterns for those spheres. In total, 105 cases were analysed, as summarised in Table 2. The testing specimens were created in the same manner as the benchmark model in the previous subsection. A loading platen was placed at each contact location and the loads were applied by moving the platens toward the centre of the particle at a constant rate of 0·1 m/s, mimicking a scenario where a particle has been 'squeezed' by its neighbouring particles. Not all the particles that were simulated experienced crushing. For some contact patterns, particularly when the contacts were 'unevenly' distributed on the particle surface, the modelled particle was observed to slip out of the platen frame without crushing. Those cases were dropped and a new contact pattern was simulated until particle crushing was observed. Examples of successfully modelled particles with loading platens are shown in Fig. 10.

Table 2. Summary of total cases for peridynamic simulation of crushing

Coordination number N_c	4	5	6	7	8	Total
Number of specimens	25	25	25	20	10	105

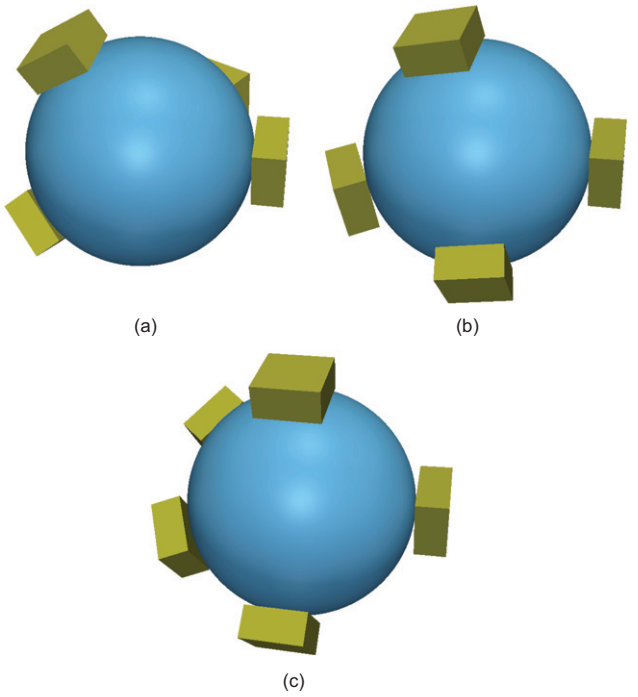

Fig. 10. Examples of modelled particle under multi-directional loadings: (a) $N_c = 4$; (b) $N_c = 5$; (c) $N_c = 6$

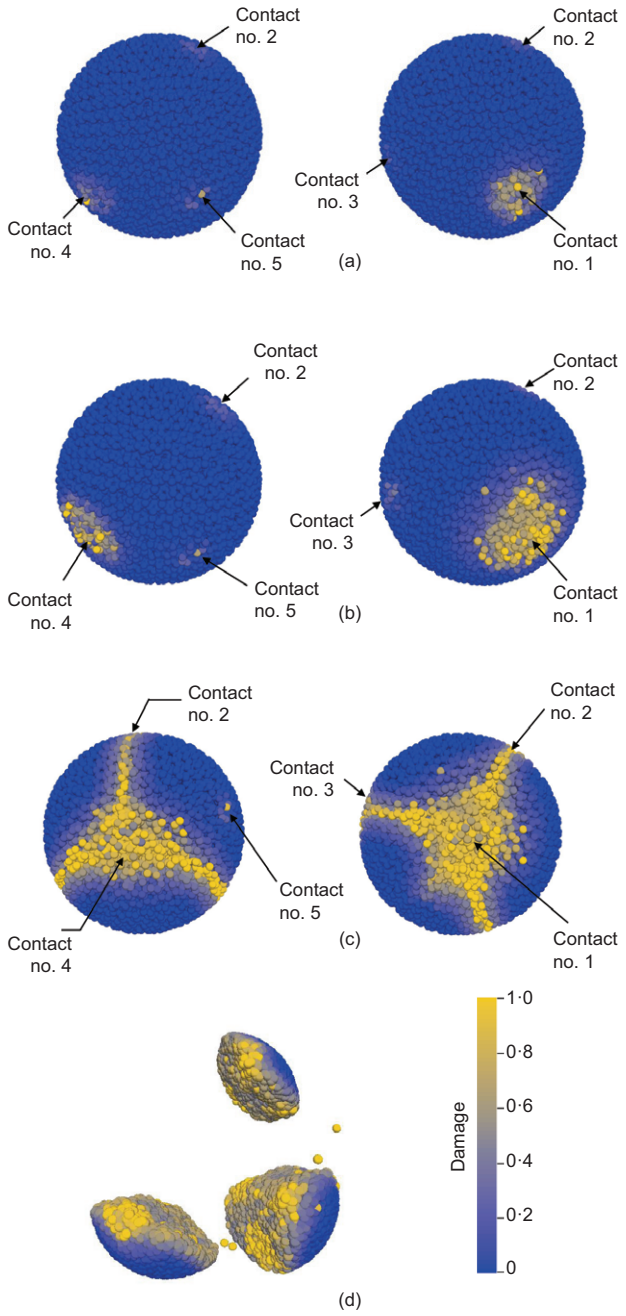

Fig. 11. Initiation and propagation of cracks inside a particle with $N_c = 5$: (a) damage initiation; (b) damage growth; (c) crack pattern; (d) broken pieces. Loading levels at conditions (a) to (d) are marked in Fig. 12

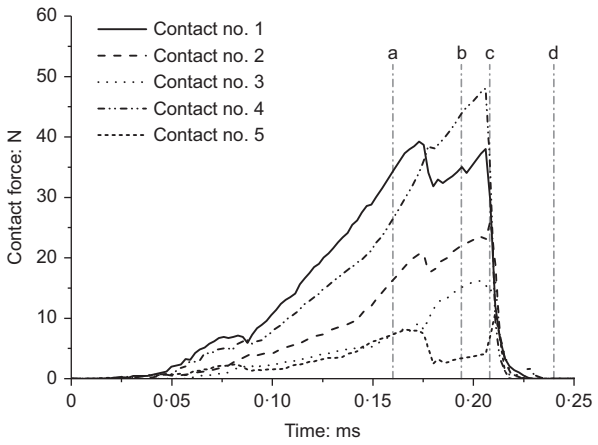

Fig. 12. Computed contact forces during loading process for the crushed particle in Fig. 11 (conditions of the particle at times a to d are shown in Fig. 11)

Figure 11 presents the simulated crushing process of a particle with five contacts and Fig. 12 shows the recorded contact forces during the loading process. Crushing of the particle underwent two stages. First, local damage was initiated and grew at the contact locations. Contacts with smaller forces generally experienced less local damage (Fig. 11(a)). The contact forces kept increasing in this stage, although some local drops could be observed, likely representing the effect of local damage. The second stage involved a sudden propagation of cracks and splitting of the particle (Fig. 11(c)). The contact forces dropped to zero after the particle had been totally crushed. From Fig. 11 it is observed that cracks are typically formed and propagated between the contacting points and crack joints are formed at some of the contact locations. For contact points with relatively small force (e.g. contact point number 5 in Fig. 11), only minor local damage was observed, indicating a relatively minor role played by such contacts in contributing to the bulky crushing of the particle. Such contacts may be seen as 'ineffective' contacts, whereas other contacts may be seen as 'effective' contacts, according to their contributions to the bulky crushing of the particle. However, upon further careful examination of the simulation results, it is deemed difficult to identify a force threshold which can delineate the 'effective' and 'ineffective' contacts pertaining to particle crushing. Fig. 11 also shows that the broken pieces are no longer in the 'orange slice' pattern as observed in uniaxial crushing tests, but vary in both size and shape. Some fine fragments were also formed during the crushing, represented by single or small clusters of material points. However, these minor fragments are not of interest within the scope of the present study and are not shown in the figure for the sake of clarity.

The pattern of cracks appeared to be affected by the coordination number, the location of contacts, as well as the magnitude of contact forces. For a given coordination number, different contact patterns exist. Even for a given contact pattern, there may be numerous possible combinations of contact forces. The present study indicates that seeking a deterministic rule of the crack pattern for a single particle with given contact pattern and contact forces would be difficult, if not completely impossible. The authors' focus is therefore placed upon summarising possible trends governing the crushing load and the crushing patterns observed from the simulations, aiming to establish a simplified crushing criterion and to explore more likely crushing patterns to facilitate the traditional discrete modelling of particle crushing. This is summarised in the following two subsections.

A simplified crushing criterion based on multiple contact crushing

As mentioned in the introduction, there have been a variety of crushing criteria proposed to predict the onset of particle crushing in discrete modelling. The common ones include the OSS criterion, the MCF criterion, the mean principal stress criterion, the major principal stress criterion and the MTS criterion. How to choose a suitable criterion in DEM modelling represents the first critical step for modellers to produce credible and convincing predictions on sand crushing. In this subsection, the authors examined the various

criteria based on their numerical results for peridynamic simulations, in an attempt to offer possible recommendations with justifications for future DEM modellers. Specifically, the contact forces at crushing were carefully extracted from the simulation results for the different cases and were then used to correlate with the crushing threshold of the OSS, the MCF, the mean principal stress, the major principal stress and the MTS for assessments. Additionally, the discussion is extended to the fracture energy of single particles by extracting the strain energy information from the peridynamic models.

OSS criterion. The OSS criterion states that crushing occurs when the octahedral shear stress reaches a critical level. The OSS in a particle is calculated by

$$q = \frac{1}{3}\sqrt{(\sigma_1 - \sigma_2)^2 + (\sigma_2 - \sigma_3)^2 + (\sigma_1 - \sigma_3)^2} \quad (9)$$

where σ_1, σ_2, σ_3 are the principal stresses calculated from a stress tensor $\boldsymbol{\sigma}_{ij} = (R/V)\sum_{c=1}^{n_c} \boldsymbol{n}_i^{(c)} F_j^{(c)}$ in which R is the radius of the particle, V represents the volume of the particle, n_c is the number of contacts, $\boldsymbol{n}_i^{(c)}$ is the normal vector at contact c and $F_j^{(c)}$ is the external force at contact c. The criterion is indeed regarded as equivalent to the well-known von Mises failure criterion, which is often applied for shear-dominated failures.

To examine the performance of the OSS criterion under different loading conditions, the crushing threshold of OSS was calculated using the crushing forces obtained from the peridynamic simulations, and the results are plotted against the coordination number in Fig. 13. The following observations were made.

(*a*) The crushing thresholds corresponding to each coordination number exhibit obvious dispersion. However, this is not surprising as the criterion is, after all, a large simplification of the complex stress field in the particle, and a similar phenomenon can be expected for other simplified crushing criteria as well. The trend of the crushing thresholds exhibited by the mean and median values is of most interest here, as it represents the overall applicability of the criterion.

(*b*) As a general trend, the crushing threshold of OSS decreases with increasing coordination number. Under multi-directional loadings ($4 \leq N_c \leq 8$), the crushing threshold can be as small as half or a third of that under uniaxial loadings. This implies that using the uniaxial crushing test data to determine the crushing level under multi-directional loadings may overestimate the crushing resistance of a particle. The effect of coordination number should therefore be considered when using the OSS criterion.

(*c*) When a particle is subject to more contacts (e.g. $6 \leq N_c \leq 8$), the mean/median crushing threshold of OSS tends to be steady, indicating a better applicability of the criterion under high coordination numbers. This is probably because the crushing under high coordination number is mainly governed by shearing, whereas the crushing under low coordination number is more tension driven or in a mixed mode.

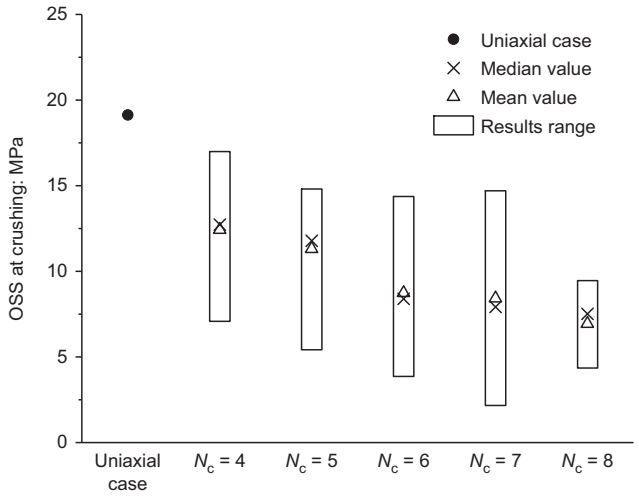

Fig. 13. OSS at crushing plotted against N_c

MCF criterion. The MCF criterion states that crushing occurs when the MCF applied to a particle reaches a critical level. The criterion was widely adopted for its simplicity. Evidence that supports such a criterion can be found in some theoretical and experimental studies. For instance, Russell & Wood (2009) used a modified von Mises failure criterion (Christensen, 2000) to study the failure of a sphere under uniaxial loadings and found that failure initiates just underneath the contact point. Hence, the initiation of failure largely depends on the magnitude of the contact force at that contact point. Consequently, this leads to the conclusion that the crushing of the particle is mainly determined by the MCF on the particle, and the failure would initiate near the contact point where the MCF is present. In relation to experimental work, direct verification of the MCF criterion is not available, probably owing to the difficulties in measuring forces at contact points. Nevertheless, some observations from experiments indirectly support such a failure criterion. Gundepudi *et al*. (1997) performed a particle crushing test under both diametrical loadings and multi-axial loadings and reported that fracture always initiated from the vicinity of the contact locations. Wang & Coop (2016) also observed that failure of LBS particles tends to initiate more often from the vicinity of the top and bottom contact points. Such findings confirmed the theoretical study by Russell & Wood (2009) and supported the MCF criterion in determining particle crushing. However, different failure mechanisms may exist. Todisco *et al*. (2017) performed crushing tests for particles under multiple contacts and observed that failure of a particle may initiate away from contact locations. Such phenomena may be a result of complex particle morphologies, which lead to great variations in the internal stress field within the particle. The applicability of the MCF criterion for such cases is, however, unclear.

Here the MCF criterion is further examined in Fig. 14 with the MCF at crushing obtained from the present authors' peridynamic simulations. Evidently, the criterion demonstrates a good applicability. The crushing threshold is not apparently affected by the coordination number. The mean and median values of the crushing threshold range between 40 N and 50 N for all cases of coordination number, and they appear to be only slightly lower than the crushing threshold under uniaxial loading. In most cases, assuming a constant crushing force appears to be rather effective and straightforward, while providing reasonable accuracy. Similarly to the previous studies on the OSS criterion, variation in the crushing threshold is observed, and it is likely to be a result of different contact locations and contact forces.

Mean and major principal stress criteria. The mean principal stress criterion and major principal stress criterion

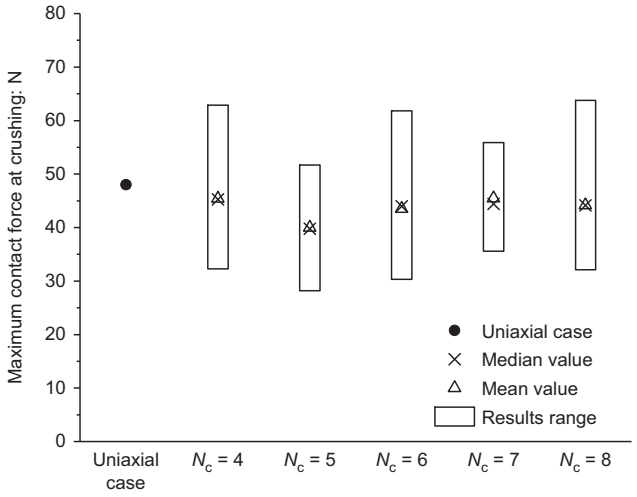

Fig. 14. Maximum contact force at crushing plotted against N_c

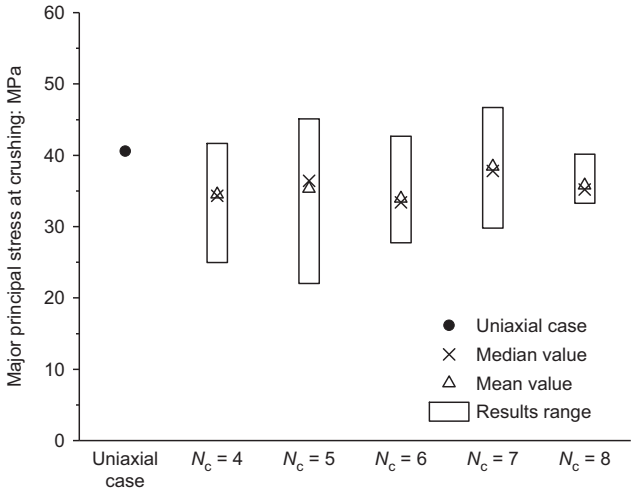

Fig. 16. Major principal stress at crushing plotted against N_c

define the crushing threshold of a particle in terms of mean principal stress and major principal stress, respectively. The principal stresses are calculated according to the stress tensor defined earlier. The two criteria were not seen often in the literature, probably owing to lack of supporting evidence. In particular, both criteria allow a particle to break under hydrostatic conditions, which appears to be unrealistic. Nevertheless, the two criteria are included here for a complete assessment of existing crushing criteria.

The mean principal stresses at crushing obtained from peridynamic models are plotted against the coordination number in Fig. 15. The crushing threshold generally increases with the coordination number and becomes steady when N_c is greater than 6. Notably, the crushing threshold for $N_c = 7$ and 8 is about twice that under uniaxial loadings, indicating again the significant underestimation it may cause if the uniaxial crushing strength is used for multi-directional loading scenarios.

The major principal stresses at crushing plotted against coordination number are shown in Fig. 16. The criterion exhibited a reasonable performance in general. The crushing threshold for particles under different loading conditions may be approximated using a constant value. It appears that the crushing threshold under uniaxial loadings tends to be higher than those under multi-directional loadings, although the difference is not significant. The mean and median values of crushing thresholds fluctuate between 32 MPa and 41 MPa for the modelled particles.

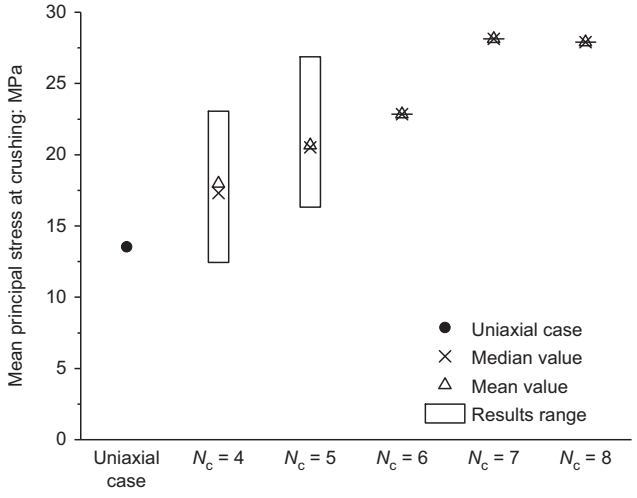

Fig. 15. Mean principal stress at crushing plotted against N_c

Comparison of the four criteria. First, the criteria are compared on performance of crushing threshold. When using the four crushing criteria discussed above, a constant crushing threshold was often adopted with the underlying assumption that the crushing level under uniaxial loadings is applicable for multi-directional loading conditions. In practice, the crushing threshold is often determined based on uniaxial crushing test results. Therefore, the performance of a crushing criterion can be rated by the variation in crushing levels between the multi-directional loading conditions and the uniaxial loading condition. Here a comparison of the four criteria was performed by assessing such variations. For each criterion, the crushing level was first extracted from the peridynamic model for the uniaxial loading case, and this was regarded as the selected crushing threshold (s_p) for the particle. Second, crushing levels were obtained from peridynamic models for the multi-directional loading cases, and these are regarded as the 'actual' crushing level of the particle (s_t). A relative difference ε between s_t and s_p can be calculated by

$$\varepsilon = \frac{|s_p - s_t|}{s_p} \times 100\% \tag{10}$$

The calculated ε indicates the performance of a criterion. A preferred criterion would be featured by a small ε for most cases, whereas a poorly performing criterion would exhibit large ε for most cases.

A comparison of the four investigated crushing criteria is presented in Fig. 17. The horizontal axis represents the relative difference in crushing levels calculated using the above equation, whereas the vertical axis indicates the percentage of cases that fall within the relative difference. The following findings are made.

(*a*) Under the MCF criterion, the relative difference is less than 10% for almost half of the cases, less than 20% in more than 70% of the cases and less than 30% in about 90% of the cases. Almost all cases are covered by a relative difference of 40%. This criterion in general offers better performance over the other criteria.
(*b*) The major principal stress criterion shows a similar performance when compared with the MCF criterion.

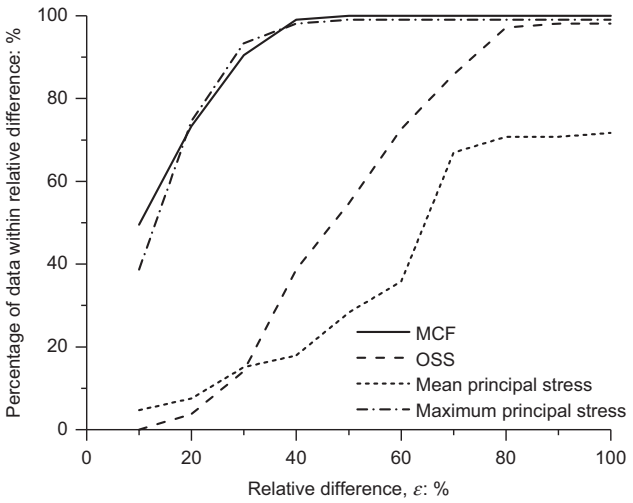

Fig. 17. Comparison of existing crushing criteria

About 40% of the cases fall within 10% relative difference. More than 70% and 90% of the cases fall within 20% and 30% relative difference, respectively; almost all cases have a relative difference of no more than 40%.

(*c*) The OSS criterion and the mean principal stress criterion show relatively unsatisfactory performance. Under both criteria, more than 80% of the cases have a relative difference of more than 30%. The performance of these criteria may be improved, as discussed before, by properly considering the effect of coordination number on the crushing threshold.

Second, a discussion of the macroscopic implications is presented. Here the authors take a further step to discuss the implications of the above findings on particle size distribution, which is an important aspect of the macroscopic properties of sand. It is known that the size distribution of particles in a crushing process follows a fractal rule (Turcotte, 1986; McDowell *et al*., 1996), in which the number of particles larger than a certain size has a power law relation to that size. Naturally, the size of particles tends to disperse during successive crushing processes (Fukumoto, 1992). The fractal feature was used to examine how reasonable the numerical modelling of particle crushing is (de Bono & McDowell, 2016). A proper single particle crushing criterion must not obstruct the formation of the fractal size distribution. In numerical modelling, a crushing criterion is usually used in conjunction with the Weibull distribution of particle strength, which also takes into account the effect of particle size (Weibull, 1951; Nakata *et al*., 1999). The Weibull distribution describes a statistical rule on the strengths of particles which is essentially a natural feature of sand. The size effect accounts for the fact that larger particles typically possess more and larger micro defects, whereas smaller particles tend to be more intact in general, thus it assigns higher strength to smaller particles and lower strength to larger particles. The selected particle crushing criterion and the Weibull strength distribution together decide the crushing of single particles, and ultimately affect the particle size distribution in a successive crushing process of sand.

The performances of the four crushing criteria with respect to particle size distribution have been examined by de Bono & McDowell (2016) using DEM. They found that the OSS criterion and MCF criterion resulted in a fractal distribution of particle size after normal compression of a sand sample, whereas the mean principal stress criterion led to poor macroscopic results and the major principal stress criterion exhibited an intermediate performance. Indeed, the present authors' findings also indicated that the mean principal stress criterion would be unlikely to lead to a fractal distribution of particle size. Under such a criterion, based on the current findings, the model tends to underestimate the crushing level of particles, particularly those large ones that bear more contacts, thus making them easier to break. Consideration of the size effect would further reduce the strength of large particles and make them more susceptible to crushing. Meanwhile, large particles typically bear more and stronger contact forces and the mean principal stress is expected to be relatively high. As a result, the large particles cannot sustain increasing load and will continue to evolve into small fragments, which tends to reduce the dispersion of particle size and prevent the formation of a fractal particle size distribution. As for the other three crushing criteria, the present authors' findings did not show any apparent qualitative sign that the fractal particle size distribution is obstructed. Under the OSS criterion, according to the above findings, the model tends to overestimate the crushing level of particles. The larger the particle is (i.e. the more contacts in general), the larger is the overestimation. However, the large particles are usually assigned with lower strength owing to the size effect, and such consideration may in fact mitigate, at least partially, the error caused by the crushing criterion, and might eventually preserve the fractal particle size distribution. The MCF criterion is often practically interpreted in the form of stress (i.e. the force divided by the diameter squared). Based on the present study's findings, the crushing stress level under different coordination numbers would be reasonably represented by the MCF criterion. Consideration of the size effect would reduce the strength of large particles and make them easier to break. However, conversely, large particles usually experience lower stress levels (de Bono & McDowell, 2016), which makes them harder to break. Reversed condition can be expected for small particles. The competition of these effects tends to cause some large particles to be crushed due to lower strength, while preserving some of the others owing to the lower stress level experienced, and lead to a dispersed distribution of particle size. The major principal stress criterion has a similar situation to the MCF criterion, although the crushing threshold seems to be somewhat overestimated by the criterion. To sum up, it appears the mean principal stress criterion will be unlikely to lead to a fractal distribution of particle size, whereas the other three criteria do not impose, at least qualitatively, any obstruction to the formation of a fractal distribution of particle size.

MTS criterion. The MTS criterion states that a particle is crushed when the maximum internal tensile stress exceeds the tensile strength (Gundepudi *et al*., 1997; Tsoungui *et al*., 1999; Lobo-Guerrero & Vallejo, 2005). The tensile splitting failure mode may be easily formed under uniaxial loadings, providing the natural basis for a crushing criterion based on the maximum tensile stress level. Such a criterion is essentially equivalent to the MCF criterion under the uniaxial loading condition, since the maximum tensile stress is proportional to the contact force (Chau & Wei, 1999). However, its applicability may be questioned under multidirectional loadings where a particle may typically fail under shear mode or mixed tension and shear mode (Ben-Nun & Einav, 2010; Salami *et al*., 2015). Based on the contact forces at failure obtained from the current study's peridynamic simulations in conjunction with the analytical solutions derived by Zhao *et al*. (2012), it is possible to calculate the stress field inside a spherical particle and to evaluate the

resultant maximum tensile stress at crushing. However, such computations are highly expensive and a comprehensive study on the failure level of tensile stress for all the cases was deemed to be unaffordable. Nevertheless, the authors' examinations of selected cases indicated that the maximum tensile stresses at crushing obtained in this way vary significantly (Fig. 18), casting shadow on the applicability of this criterion for more general cases than uniaxial loading. In addition, there are two other notable drawbacks associated with the application of the criterion: (*a*) the analytical solution sought for the stress field distribution within a particle is sensitive to the assumptions made at contacts. Using uniform pressure or non-uniform Hertz pressure at contacts will result in great differences in the calculated maximum tensile stress inside the particle; (*b*) numerical difficulties and errors may be encountered when solving the tensile stress field near the surface of a particle (Zhao *et al*., 2012), which affects the credibility of the solution.

Fracture energy of single particles. Other than the force- and stress-based crushing criteria, the crushing threshold of a particle may also be described in terms of energy. In classical fracture mechanics, the growth of cracks is often driven by the stored elastic strain energy and external force work (Wei, 2010). For a particle crushed under compressive forces, however, the external force work does not directly lead to the extension of crack tips but is stored in the particle in the form of elastic strain energy. At the moment of crushing, the stored elastic strain energy is the main source of energy that drives the growth of cracks. The elastic strain energy needed to cause crushing of a particle is often termed the 'fracture energy'. Experimental tests have been performed to study the fracture energy of particles under uniaxial loadings (Yashima *et al*., 1987; Tavares & King, 1998). Similarly to the particle strength measured using force or stress, the fracture energy of single particles was found to follow Weibull statistics (Zhang *et al*., 2016), and it may also be linked to breakage mechanics (Einav, 2007) on a macroscopic level. Again, a question may be asked whether the crushing threshold of strain energy obtained under uniaxial loadings is applicable for particles under multi-directional loadings. Here the authors use the peridynamic modelling results to evaluate the crushing threshold under various loading conditions. In peridynamics (Silling *et al*., 2007), the elastic strain energy density at a material point is calculated by

$$W\langle \boldsymbol{x} \rangle = \frac{k\theta^2}{2} + \frac{15\mu}{2m\langle \boldsymbol{x} \rangle} \int_{\mathcal{H}_x} \omega (\underline{e}^{\mathrm{d}})^2 \, \mathrm{d}V_{x'} \tag{11}$$

The total elastic strain energy stored in the particle, E_{s}, is calculated by summarising the elastic strain energies at all material points

$$E_{\mathrm{s}} = \sum_{i=1}^{n} W\langle \boldsymbol{x}_i \rangle \cdot \mathrm{d}V_{x_i} \tag{12}$$

where n denotes the number of material points of the modelled particle. Figure 19 shows the elastic strain energy of particles at crushing calculated from the peridynamic simulation. It is observed that, for particles with $4 \leq N_{\mathrm{c}} \leq 6$, the crushing thresholds appear to reside within a narrow range with an average value near 0·5 mJ. The crushing threshold increases slightly for particles with $N_{\mathrm{c}} \geq 7$. Such an increasing trend may reflect the fact that, when a particle is subjected to more contacts, some of them may not effectively contribute to the occurrence of crushing (refer to Fig. 11) but still feed strain energy to the particle, hence resulting in a higher stored strain energy level at crushing. This is particularly true for large particles, which typically bear more contacts. The observations indicate that if a constant value of stored strain energy is used as the crushing threshold its validity may be questionable at relatively high coordination numbers. It is also noticed that there are some outlier data which cannot be reasonably approximated by a constant threshold. As an overall observation, the stored strain energy does not appear to be a quantity suitable for serving a simplified particle crushing criterion for all cases.

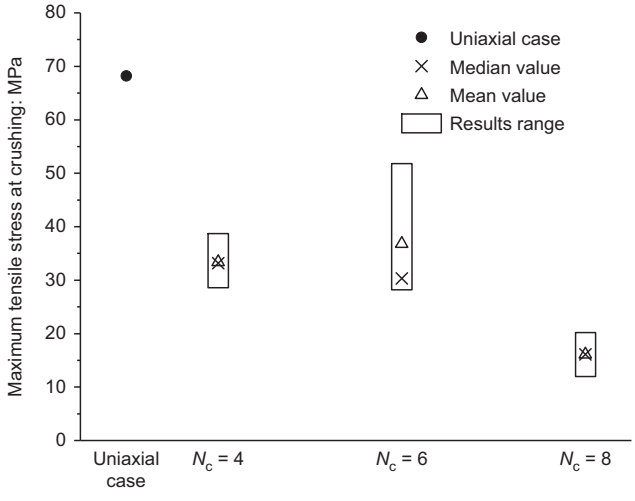

Fig. 18. Maximum tensile stress at crushing plotted against N_{c}. (Note that: (*a*) owing to excessive computational cost, in total nine cases have been calculated for the multi-directional loading condition (four for $N_{\mathrm{c}} = 4$, three for $N_{\mathrm{c}} = 6$ and two for $N_{\mathrm{c}} = 8$); (*b*) the calculation assumed uniform pressure distribution at contacts and a half-contact angle of 5°; (*c*) to save computational cost, calculation points were selected along the radius of MCF with an interval of 0·05R up to 0·9R, where R represents the radius of the sphere. Tensile stress at the sphere surface was not calculated)

Crushing pattern

Upon crushing, a particle typically breaks into a few major pieces with a great number of small fragments. Many of the fragments may be too small to be even identified by the

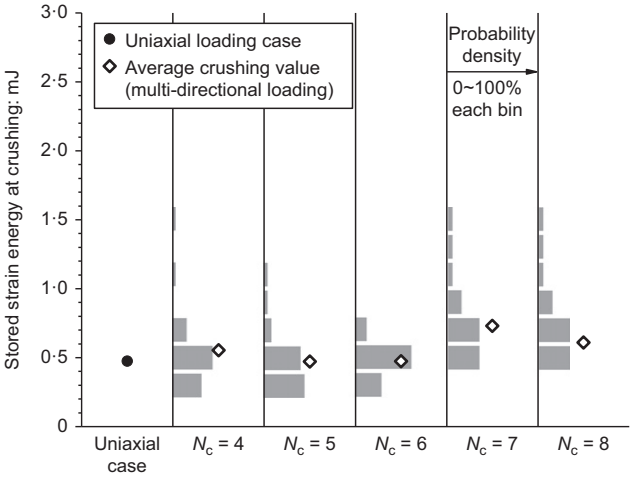

Fig. 19. Summary of crushing threshold of stored strain energy from the peridynamic simulations

naked eye. In discrete modelling of the crushing process, it is common that only the major pieces are considered while neglecting these excessively small fragments for convenience of manipulation and computational efficiency. The present study is focused on studying the major broken pieces, hereafter termed child particles. To be more specific, a child particle considered here refers to a broken piece that possesses a volume (or mass) not less than 3% of its parent particle, while those broken pieces below the threshold are considered to be trivial fragments. In practical modelling, however, this threshold can be adjusted depending on the specific materials and applications, and the density/mass of the child particles can be adjusted to account for the loss of fragments if one wishes to preserve mass conservation during the successive simulation.

For all the analysed cases, the number of child particles N_p was counted and these are summarised in Fig. 20. The results show that each analysed particle breaks into no more than seven child particles, and the average and median N_p values are between 3 and 4. It is interesting to observe the coordination number does not exhibit any apparent impact on the number of child particles. A possible reason is that when a particle is subject to multiple contacts, cracks will form first between a limited number of contacts and quickly propagate, resulting in unstable tilting or rotation of the particle, which further lead to the release and redistribution of forces at other contacts. Consequently, no new cracks will be created at other positions after the dominant, first occurring cracks dividing the particle into a few major pieces. Fig. 11 indeed demonstrates an example of such a situation. The contact number 5 of the particle bears a relatively small force during the loading process. When the bulk cracks were formed between other contacts, the particle was split and could no longer maintain its original position, thus the local damage at contact number 5 was not possible to further develop into crack surfaces. This case can indeed be considered equivalent to a four-point contact case whereby the number 5 contact does not exist at all. Likewise, if there are more contacts which only bear small forces, cracks may not develop at these contacts and the number of child particles will likely remain the same, such that more contacts do not necessarily result in more child particles.

The statistics of child particle number N_p among all the cases simulated here are summarised in Fig. 21. In the majority of cases, the number of child particles is found to be between two and five. The overall probabilities of a particle breaking into two to five child particles are observed to be similar, although the chance for producing three child particles appears to be slightly higher, which may be because

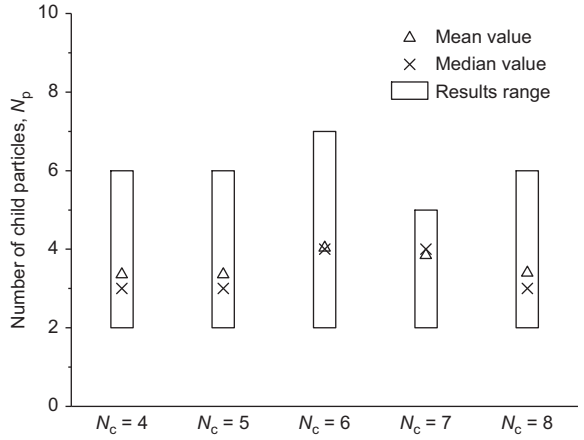

Fig. 20. Number of child particles plotted against coordination number

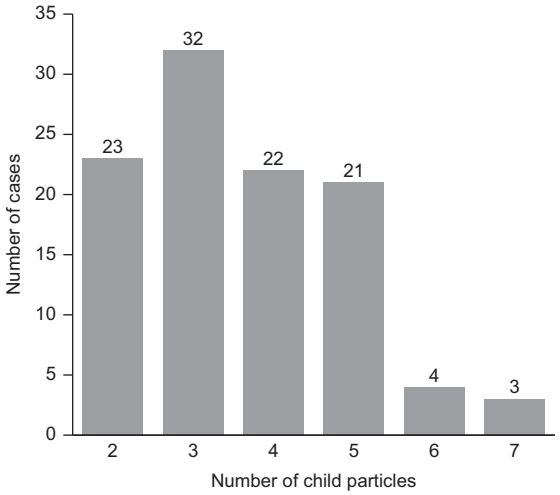

Fig. 21. Probability distribution of the number of child particles

only limited cases were studied. Practically, it may be reasonable to assume one particle crushes into two to five child particles with equal chances.

In addition, the volumes of the child particles were also measured for cases with $N_p = 2$ to 5. The distributions of the child particle volumes, shown in Fig. 22, are evidently non-uniform. For $N_p = 2$, the most frequently occurring crushing pattern is that a particle breaks into two child particles with roughly even volumes. More than 70% of the child particles have volumes of 30 to 65% of the parent particle. The case where a particle breaks into very large and very small pieces appears to be rather scarce. The distribution of the volumes can generally be described by a normal distribution, as shown in the figure, while the measured volume data do not show a perfect fit for the normal distribution profile, probably owing to the limited modelling cases and data available. For $N_p = 3$, more than 75% of the child particles possess volumes between 5 and 40% of the parent particle. For $N_p = 4$ and 5, more than 75% of the child particles have volumes below 30% of the parent particle. The distributions for $3 \leq N_p \leq 5$ can generally be described by gamma distributions, as shown. As expected, the peak probability density moves left with the increase in N_p, indicating smaller mean volume when there are more child particles produced. Moreover, when there are more child particles, their volumes tend to be less dispersive and more concentrated in a narrow range. In other words, the volumes of child particles tend to be more similar to one another when there are more child particles.

In discrete-element modelling, one may opt to assume the volumes of child particles following the distributions presented in the above figures. A more simplified approach, as has been adopted in many past studies, is to assume that a particle breaks into equal-sized child particles. Such an assumption appears to be more appropriate for cases where there are more child particles (e.g. $N_p = 4$ and 5), for which the child particle volumes are less dispersive. When there are only two or three child particles, this assumption tends to be less accurate. Nevertheless, past studies (de Bono & McDowell, 2016) have shown that assuming equal-sized child particles can lead to reasonable macroscopic results. It may therefore be expected that assuming equal-sized child particles does not impose an apparent error on the macroscopic mechanical results from numerical modelling, unless the final grain size distribution is a major concern, such as the comminution in the mining industry.

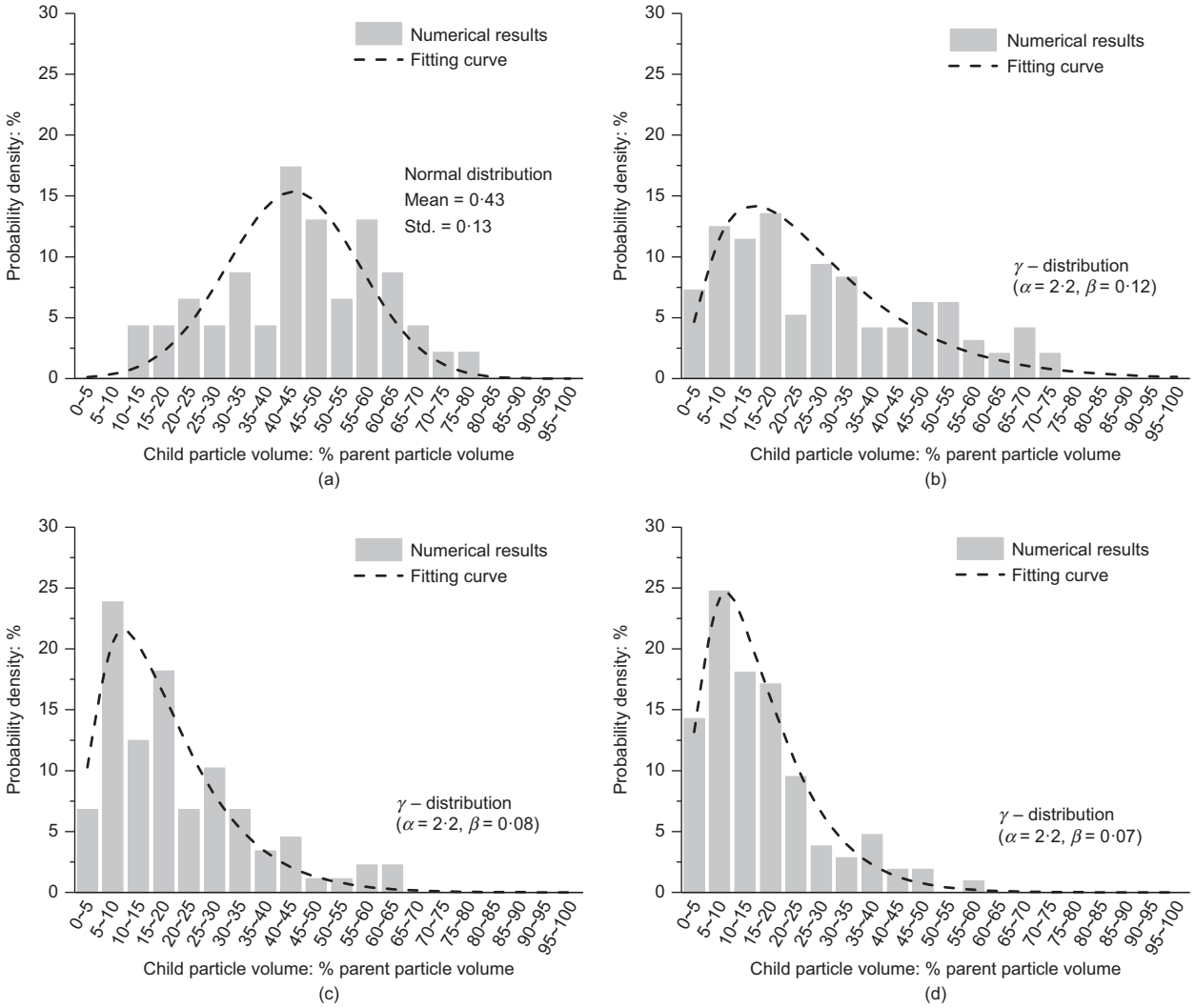

Fig. 22. Distribution of volume of child particles: (a) $N_p = 2$; (b) $N_p = 3$; (c) $N_p = 4$; (d) $N_p = 5$

CONCLUSIONS

This paper has presented a peridynamic study on the crushing criteria and crushing pattern of single sand particles under various loading conditions. Spherical, isotropic and homogeneous silica sand particles subjected to elastic brittle failure were considered in the crushing analysis. For a particle crushed under uniaxial loadings, the peridynamic method demonstrated its capability in reasonably predicting the crushing load and capturing the initiation of damage and propagation of cracks. The method was further extended to model single particle crushing under multi-directional loading conditions. The following major conclusions are drawn.

(*a*) Among the existing crushing criteria, the MCF criterion is found to have the best agreement with the peridynamic results. It appears that the MCF at crushing is not obviously affected by the coordination number. As such, the criterion is applicable to both uniaxial and multi-directional loading conditions and the crushing threshold shows relatively good consistency over the different cases examined in the present study. The criterion achieves a relative error of less than 10% in half of the studied cases, less than 20% in more than 70% of the studied models and less than 30% in more than 90% of the studied cases. The performances of other crushing criteria are found to be less satisfactory compared to the MCF.

(*b*) A particle typically breaks into two to five child particles with similar chances. The average and median values of child particle number N_p are between 3 and 4, and N_p is not apparently affected by the coordination number of a particle.

(*c*) The examination of the crushed particles by peridynamic simulations shows that the volumes of child particles are not uniformly distributed. When $N_p = 2$, the distribution of the volumes of child particles can generally be described by a normal distribution, whereas for $3 \leq N_p \leq 5$ it can generally be described by gamma distributions. With more child particles, the distribution of their volumes appears to be less dispersive and concentrate in a smaller range. Assuming equal-sized child particles may be a reasonable simplification when the child particle number N_p is large, but appears to be less accurate when N_p is small. However, it is noted that such an assumption can still produce reasonable macroscopic results according to other studies.

(*d*) For discrete-element modelling, when particle crushing needs to be considered, the MCF criterion is recommended in conjunction with an assumption that a particle breaks into two to five equal-sized child particles with equal chances. Such an approach presents a simplified but efficient way to model particle crushing, and offers reasonable accuracy based on the numerical investigation on the single

particle level presented in this paper, as well as in past studies.

This paper therefore serves as a numerical investigation on single sand particle crushing behaviour under various loading conditions, to complement existing experimental testing results on crushing of single particles. It is expected to offer insight into the crushing criterion and crushing pattern of single particles, which will serve as useful information to facilitate future discrete modelling of particles where consideration of crushing is important. Nevertheless, the following limitations should be noted. (*a*) The study has considered the crushing of a perfectly idealised, spherical, homogeneous particle, whereas in reality the breakage may occur more often on non-spherical, defect-bearing particles, as well as particles in a successive crushing process. Discrete modelling of successive crushing in an assembly of irregularly shaped particles is a challenging future task to be tackled. Other factors such as conditions at contact may also influence the crushing characteristics of a particle and this is worth a more detailed study in the future. (*b*) The 105 cases of multiple-contact peridynamic simulations may not be adequate for the present observations to be statistically representative. More numerical and experimental tests should be performed to gain substantial validating data. (*c*) Particle crushing in the presence of other phases and factors, such as fluid, chemically active agents and temperature changes, may find more interesting applications in areas other than geotechnical engineering and can also be considered in the future.

ACKNOWLEDGEMENTS

The authors appreciate the constructive comments and suggestions offered by Professor Matthew R. Coop of University College London. The study was financially supported by the National Natural Science Foundation of China (by project no. 51679207) and the Research Grants Council of Hong Kong under the Theme-based Research Scheme (by project no. T22-603/15-N) and the General Research Fund scheme (Grant No. 16210017). The first author also acknowledges financial support from the Hong Kong Ph.D. Fellowship Scheme funded by the Research Grants Council of Hong Kong.

NOTATION

$\boldsymbol{b}$	body force
c	contact point
d_{pi}	contact distance
$\mathrm{d}V$	volume of a material point
E_{s}	total elastic strain energy
$\underline{e}$, $\underline{e}^{\mathrm{i}}$, $\underline{e}^{\mathrm{d}}$	extension scalar state, its isotropic and deviatoric components
F	external force at contact point
F_{T}, F_{N}	tangential and normal contact force
f	coefficient of friction
f_s	contact force density
G_{c}	critical energy release rate
g	damage of bond
$\mathcal{H}_x$	family of material point $\boldsymbol{x}$
k	contact stiffness
m	weighted volume
N_{c}, n_{c}	coordination number
N_{p}	number of child particles
n	number of material points of the modelled particle
$\boldsymbol{n}^{(c)}$	normal vector at contact point
q	octahedral shear stress
R, V	radius and volume of a particle
s_{c}	critical stretch
s_{p}	crushing level under uniaxial loading
s_{t}	crushing level under multi-directional loading
T	time
$\boldsymbol{T}$	peridynamic force state
$\underline{t}$	scalar force state
$\boldsymbol{u}$	displacement vector
$\ddot{\boldsymbol{u}}$	acceleration
V	velocity
W	elastic strain energy density
$\underline{x}$	position scalar state
$\boldsymbol{Y}$	deformation vector
$\boldsymbol{y}$	current location of material point
Δx	material point spacing
δ	horizon
ε	relative difference
θ	dilation
μ, K	shear and bulk modulus
$\boldsymbol{\xi}$	bond vector
ρ	density
σ_1, σ_2, σ_3	principal stress components
$\boldsymbol{\sigma}_{ij}$	stress tensor
ϕ	damage of material point
ω	influence function

REFERENCES

Antonyuk, S., Tomas, J., Heinrich, S. & Morl, L. (2005). Breakage behaviour of spherical granulates by compression. *Chem. Engng Sci.* **60**, No. 14, 4031–4044.

Baydoun, M. & Fries, T. P. (2012). Crack propagation criteria in three dimensions using the XFEM and an explicit–implicit crack description. *Int. J. Fracture* **178**, No. 1–2, 51–70.

Ben-Nun, O. & Einav, I. (2010). The role of self-organization during confined comminution of granular materials. *Phil. Trans. A. Math. Phys. Engng Sci.* **368**, No. 1910, 231–247.

Bouchard, P. O., Bay, F. & Chastel, Y. (2003). Numerical modelling of crack propagation: automatic remeshing and comparison of different criteria. *Comput. Methods Appl. Mech. Engng* **192**, No. 35–36, 3887–3908.

Brace, W. F. & Walsh, J. B. (1962). Some direct measurements of the surface energy of quartz and orthoclase. *Am. Mineralogist* **47**, No. 9–10, 1111–1122.

Brosh, T., Kalman, H. & Levy, A. (2011). Fragments spawning and interaction models for DEM breakage simulation. *Granular Matter* **13**, No. 6, 765–776.

Chau, K. T. & Wei, X. X. (1999). Spherically isotropic, elastic spheres subject to diametral point load strength test. *Int. J. Solids Structs* **36**, No. 29, 4473–4496.

Cheng, Y. P., Nakata, Y. & Bolton, M. D. (2003). Discrete element simulation of crushable soil. *Géotechnique* **53**, No. 7, 633–641, https://doi.org/10.1680/geot.2003.53.7.633.

Christensen, R. M. (2000). Yield functions, damage states, and intrinsic strength. *Math. Mech. Solids* **5**, No. 3, 285–300.

Cil, M. B. & Alshibli, K. A. (2012). 3D assessment of fracture of sand particles using discrete element method. *Géotechnique Lett.* **2**, No. 3, 161–166, https://doi.org/10.1680/geolett.12.00024.

Cil, M. B. & Alshibli, K. A. (2014). 3D evolution of sand fracture under 1D compression. *Géotechnique* **64**, No. 5, 351–364, https://doi.org/10.1680/geot.13.P.119.

Cil, M. B. & Buscarnera, G. (2016). DEM assessment of scaling laws capturing the grain size dependence of yielding in granular soils. *Granular Matter* **18**, No. 3, article 36.

Couroyer, C., Ning, Z. & Ghadiri, M. (2000). Distinct element analysis of bulk crushing: effect of particle properties and loading rate. *Powder Technol.* **109**, No. 1–3, 241–254.

Cundall, P. A. & Strack, O. D. L. (1979). A discrete numerical model for granular assemblies. *Géotechnique* **29**, No. 1, 47–65, https://doi.org/10.1680/geot.1979.29.1.47.

Daux, C., Moes, N., Dolbow, J., Sukumar, N. & Belytschko, T. (2000). Arbitrary branched and intersecting cracks with the extended finite element method. *Int. J. Numer. Methods Engng* **48**, No. 12, 1741–1760.

De Bono, J. & McDowell, G. (2016). Particle breakage criteria in discrete-element modelling. *Géotechnique* **66**, No. 12, 1014–1027, https://doi.org/10.1680/jgeot.15.P.280.

Domenico, S. N. (1977). Elastic properties of unconsolidated porous sand reservoirs. *Geophysics* **42**, No. 7, 1339–1368.

Einav, I. (2007). Breakage mechanics – part I: theory. *J. Mech. Phys. Solids* **55**, No. 6, 1274–1297.

Erdoğan, S. T., Forster, A. M., Stutzman, P. E. & Garboczi, E. J. (2017). Particle-based characterization of Ottawa sand: shape, size, mineralogy, and elastic moduli. *Cem. Concr. Composites* **83**, 36–44.

Fukumoto, T. (1992). Particle breakage characteristics of granular soils. *Soils Found.* **32**, No. 1, 26–40.

Gundepudi, M. K., Sankar, B. V., Mecholsky, J. J. Jr and Clupper, D. C. (1997). Stress analysis of brittle spheres under multiaxial loading. *Powder Technol.* **94**, No. 2, 153–161.

Guo, N. & Zhao, J. (2013). The signature of shear-induced anisotropy in granular media. *Comput. Geotech.* **47**, 1–15.

Ha, Y. D. & Bobaru, F. (2010). Studies of dynamic crack propagation and crack branching with peridynamics. *Int. J. Fracture* **162**, No. 1–2, 229–244.

Hanley, K. J., O'Sullivan, C. & Huang, X. (2015). Particle-scale mechanics of sand crushing in compression and shearing using DEM. *Soils Found.* **55**, No. 5, 1100–1112.

Holtzman, R., Silin, D. B. & Patzek, T. W. (2009). Mechanical properties of granular materials: a variational approach to grain-scale simulations. *Int. J. Numer. Analyt. Methods Geomech.* **33**, No. 3, 391–404.

Huang, D., Lu, G. & Liu, Y. (2015). Nonlocal peridynamic modeling and simulation on crack propagation in concrete structures. *Math. Probl. Engng* **2015**, article ID 858723.

Jaeger, J. C. (1967). Failure of rocks under tensile conditions. *Int. J. Rock Min. Sci.* **4**, No. 2, 219–227.

Kilic, B. & Madenci, E. (2009). Prediction of crack paths in a quenched glass plate by using peridynamic theory. *Int. J. Fracture* **156**, No. 2, 165–177.

Lai, X., Liu, L., Li, S., Zeleke, M., Liu, Q. & Wang, Z. (2018). A non-ordinary state-based peridynamics modeling of fractures in quasi-brittle materials. *Int. J. Impact Engng* **111**, 130–146.

Lee, D. M. (1992). *The angles of friction of granular fills*. PhD dissertation, Cambridge University, Cambridge, UK.

Li, H., McDowell, G. R. & Lowndes, I. (2013). Discrete-element modelling of rock breakage using dense random packing agglomerates. *Géotechnique Lett.* **3**, No. 3, 98–102, https://doi.org/10.1680/geolett.13.00040.

Liu, M., Wang, Q. & Lu, W. (2017). Peridynamic simulation of brittle-ice crushed by a vertical structure. *Int. J. Nav. Archit. Ocean Engng* **9**, No. 2, 209–218.

Lobo-Guerrero, S. & Vallejo, L. (2005). Crushing a weak granular material: experimental numerical analyses. *Géotechnique* **55**, No. 3, 245–249, https://doi.org/10.1680/geot.2005.55.3.245.

Madenci, E. & Oterkus, E. (2014). *Peridynamic theory and its applications*. New York, NY, USA: Springer.

McDowell, G. R. (2002). On the yielding and plastic compression of sand. *Soils Found.* **42**, No. 1, 139–145.

McDowell, G. R. & de Bono, J. P. (2013). On the micro mechanics of one-dimensional normal compression. *Géotechnique* **63**, No. 11, 895–908, https://doi.org/10.1680/geot.12.P.041.

McDowell, G. R., Bolton, M. D. & Robertson, D. (1996). The fractal crushing of granular materials. *J. Mech. Phys. Solids* **44**, No. 12, 2079–2102.

Mitchell, J. M., Silling, S. A. & Littlewood, D. J. (2015). A position-aware linear solid constitutive model for peridynamic. *J. Mech. Mater. Structs* **10**, No. 5, 539–557.

Nakata, Y., Hyde, A. F. L., Hyodo, M. & Murata, H. (1999). A probabilistic approach to sand particle crushing in the triaxial test. *Géotechnique* **49**, No. 5, 567–583, https://doi.org/10.1680/geot.1999.49.5.567.

Nakata, Y., Kato, Y., Hyodo, M., Hyde, A. F. L. & Murata, H. (2001). One-dimensional compression behavior of uniformly graded sand related to single particle crushing strength. *Soil Found.* **41**, No. 2, 39–51.

Parks, G. A. (1984). Surface and interfacial free energies of quartz. *J. Geophys. Res.: Solid Earth (1978–2012)* **89**, No. B6, 3997–4008.

Parks, M. L., Littlewood, D. J., Mitchell, J. A. & Silling, S. A. (2012). *Peridigm users' guide*, Sandia Report. Albuquerque, NM, USA: Sandia National Laboratories.

Rabczuk, T. & Ren, H. (2017). A peridynamics formulation for quasi-static fracture and contact in rock. *Engng Geol.* **225**, No. 20, 42–48.

Russell, A. R. & Wood, D. M. (2009). Point load tests and strength measurements for brittle spheres. *Int. J. Rock Mech. Min. Sci.* **46**, No. 2, 272–280.

Salami, Y., Dano, C., Hicher, P. Y., Colombo, G. & Denain, P. (2015). The effects of the coordination on the fragmentation of a single grain. *IOP Conf. Ser.: Earth Environ. Sci.* **26**, No. 1, 012015.

Salman, A. D., Gorham, D. A. & Verba, A. (1995). A study of solid particle failure under normal and oblique impact. *Wear* **186–187**, Part 1, 92–98.

Silling, S. A. (2000). Reformulation of elasticity theory for discontinuities and long-range forces. *J. Mech. Phys. Solids* **48**, No. 1, 175–209.

Silling, S. A. & Askari, E. (2005). A meshfree method based on the peridynamic model of solid mechanics. *Comput. Structs* **83**, No. 17–18, 1526–1535.

Silling, S. A., Epton, M., Weckner, O., Xu, J. & Askari, A. (2007). Peridynamics states and constitutive modeling. *J. Elasticity* **88**, No. 2, 151–184.

Spencer, J. W. Jr., Cates, M. E. & Thompson, D. D. (1994). Frame moduli of unconsolidated sands and sandstones. *Geophysics* **59**, No. 9, 1352–1361.

Tavares, L. M. & King, R. P. (1998). Single-particle fracture under impact loading. *Int. J. Miner. Processing* **54**, No. 1, 1–28.

Todisco, M. C., Wang, W., Coop, M. R. & Senetakis, K. (2017). Multiple contact compression tests on sand particles. *Soils Found.* **57**, No. 1, 126–140.

Tsoungui, O., Vallet, D. & Charmet, J. C. (1999). Numerical model of crushing of grains inside two-dimensional granular materials. *Powder Technol.* **105**, No. 1–3, 190–198.

Turcotte, D. L. (1986). Fractals and fragmentation. *J. Geophys. Res.* **91**, No. B2, 1921–1926.

Wang, W. & Coop, M. R. (2016). An investigation of breakage behaviour of single sand particle using a high-speed microscope camera. *Géotechnique* **66**, No. 12, 984–998, https://doi.org/10.1680/jgeot.15.P.247.

Wang, J. F. & Yan, H. B. (2011). 3D DEM simulation of crushable granular soils under plane strain compression condition. *Procedia Engng* **14**, 1713–1720.

Warren, T. L., Silling, S. A., Askari, A., Weckner, O., Epton, M. A. & Xu, J. (2009). A non-ordinary state-based peridynamic method to model solid material deformation and fracture. *Int. J. Solids Structs* **46**, No. 5, 1186–1195.

Wei, P. (2010). *Fracture mechanics: integration of mechanics, materials science, and chemistry*. New York, NY, USA: Cambridge University Press.

Weibull, W. (1951). A statistical distribution function of wide applicability. *J. Appl. Mech.* **18**, 293–297.

Xu, D., Liu, Z., Liu, X., Zeng, Q. & Zhuang, Z. (2014). Modeling of dynamic crack branching by enhanced extended finite element method. *Comput. Mech.* **54**, No. 2, 489–502.

Yashima, S., Kanda, Y. & Sano, S. (1987). Relationships between particle size and fracture energy or impact velocity required to fracture as estimated from single particle crushing. *Powder Technol.* **51**, No. 3, 277–282.

Zeleny, R. A. & Piret, E. L. (1962). Dissipation of energy in single particle crushing. *Ind. Engng Chem. Process Des. Dev.* **1**, No. 1, 37–41.

Zhang, Y. D., Buscarnera, G. & Einav, I. (2016). Grain size dependence of yielding in granular soils interpreted using fracture mechanics, breakage mechanics and Weibull statistics. *Géotechnique* **66**, No. 2, 149–160, https://doi.org/10.1680/jgeot.15.P.119.

Zhao, S., Gan, Y. & Kamlah, M. (2012). Spherical ceramic pebbles subjected to multiple non-concentrated surface loads. *Int. J. Solids Structs* **49**, No. 3–4, 658–671.

Zhao, B., Wang, J., Coop, M. R., Viggian, G. & Jiang, M. (2015). An investigation of single sand particle fracture using X-ray micro-tomography. *Géotechnique* **65**, No. 8, 625–641, https://doi.org/10.1680/geot.4.P.157.

Zhou, X. P. & Shou, Y. D. (2017). Numerical simulation of failure of rock-like material subjected to compressive loads using improved peridynamic method. *Int. J. Geomech.* **17**, No. 3, 04016086.

Zhou, B., Wang, J. & Wang, H. (2014). A new probabilistic approach for predicting particle crushing in one-dimensional compression of granular soil. *Soils Found.* **54**, No. 4, 833–844.